ChemComm

COMMUNICATION

View Article Online
View Journal | View Issue

Cite this: *Chem. Commun.*, 2025, **61**, 3151

Received 15th October 2024,
Accepted 13th January 2025

DOI: 10.1039/d4cc05484a

rsc.li/chemcomm

An aqueous zinc-ion battery with an organic–inorganic nanohybrid cathode featuring high operating voltage and long-term stability†

Saad Zafar, Muskan Sharma, Soumyasri Nikhilesh Mahapatra and Bimlesh Lochab *

Cathode materials with both high capacity and high operating voltage are essential for advancing aqueous zinc-ion batteries (ZIBs). Conventional high-capacity materials, such as vanadium-based compounds, typically deliver low discharge voltages. In contrast, organic cathodes show high operating voltages but often exhibit limited capacity. The present study focuses on developing hybrid cathodes composed of organic (amino PEG amine, APA) and inorganic (ammonium vanadium oxide, NVO) components, referred to as APA-NVO, featuring a dual energy-storage mechanism specifically designed to achieve a wide operating voltage of 1.9 V and provide exceptionally durable ZIBs.

Lithium-ion batteries (LIBs) continue to have a significant position in the energy storage market. However, their progress is impeded by expensive raw materials and inherent safety issues.[1–3] Rechargeable multivalent ion batteries, including zinc-ion batteries (ZIBs), aluminum-ion batteries (AIBs), and magnesium-ion batteries (MIBs), have gained significant interest due to their high volumetric energy density. Specifically, ZIBs, AIBs, and MIBs can deliver volumetric capacities of 5851 mA h mL^{-1}, 8046 mA h mL^{-1}, and 3833 mA h mL^{-1}, respectively, based on the metal anode.[4–7] Notably, the zinc anode possesses a higher redox potential (E_0 = −0.76 V *vs.* SHE, standard hydrogen electrode) in comparison to other metal anodes, endowing it with suitability for use in aqueous battery systems. Substituting organic electrolytes with aqueous ones alleviates the rising environmental and safety concerns along with the cost. Worldwide, benign-by-design approaches are highly acknowledged, making the development of high-performance ZIBs for large-scale energy storage particularly relevant. These batteries offer several advantages, including safety, abundant zinc sources, environmental friendliness, and high energy density.[8–10]

Materials Chemistry Laboratory, Department of Chemistry, School of Natural Sciences, Shiv Nadar Institution of Eminence, Gautam Buddha Nagar, Uttar Pradesh 201314, India. E-mail: bimlesh.lochab@snu.edu.in

† Electronic supplementary information (ESI) available. See DOI: https://doi.org/10.1039/d4cc05484a

In this regard, researchers have explored several inorganic compounds as ZIB cathodes, including manganese-based, vanadium-based, and Prussian blue equivalents.[11–13] Vanadium-based cathodes are extensively studied for their practical benefits, including low cost, high theoretical capacity, multiple oxidation states, and controllable structure.[14,15] In particular, V_2O_5 is widely used as a cathode material due to its layered structure, which provides 2D channels for rapid ion transport. However, its low electrical conductivity and restricted internal structure limit its performance in aqueous ZIBs.[16] To address this, preintercalation of various cations (*e.g.*, Li^+, Na^+, K^+, Ag^+, Co^{2+}, Ba^{2+}, Ca^{2+}, Mg^{2+}, Al^{3+}, Zn^{2+}) has been employed to engineer the interlayer space. These cations act as 'pillars,' expanding the V_2O_5 galleries, thereby widening diffusion channels and enhancing ion transport kinetics.[17] Nevertheless, while these cations form ionic connections with exposed oxygen atoms in the V_2O_5 layers, they also induce electrostatic repulsions that slow Zn^{2+} movement. Recently, hydrated NH_4^+-stabilized V_2O_5 has shown improved energy density and cycling stability. Unlike metal cations, NH_4^+ forms hydrogen bonds with V_2O_5, leading to better structural configurations and higher gravimetric capacities.[18,19]

Additionally, organic materials are emerging as promising electroactive materials due to their high operating voltage and limited phase transitions.[20,21] Their accessible redox sites enable rapid Zn^{2+} storage kinetics.[22] However, when used directly as cathodes in aqueous batteries, these materials tend to dissolve in the electrolyte.[23] Additionally, their high redox potential contributes to electrolyte decomposition.[24] An alternative approach involves using organic materials as interlayer hosts in vanadium compounds to enhance zinc storage.[25–27] Yet, these organic components primarily function by expanding interlayer spacing, rather than leveraging on their intrinsic properties. As a result, this strategy fails to address the issue of low voltage in vanadium-based cathodes.[27]

Recognizing the advantages of organic and inorganic materials in energy storage, we designed a hybrid cathode (APA-NVO) for aqueous ZIBs. This hybrid material, combining ammonium

vanadium oxide (NVO) and amino-PEG-amine (APA), offers a high operating voltage of 1.9 V, high capacity, and long cycle life. Both APA and vanadium oxide actively participate in zinc storage, enhancing the overall system performance synergistically. The resulting zinc/APA-NVO batteries demonstrated a dual energy-storage mechanism, delivering a specific capacity of up to 376.6 mA h g^{-1} at a current density of 0.1 A g^{-1}. Additionally, the battery showed exceptional cycling stability, maintaining performance over 1200 cycles at 3 A g^{-1}, facilitating rapid and reversible Zn^{2+} storage. The present work on hybrid cathodes, integrating organic and inorganic components, could accelerate the development of high-energy cathodes for aqueous ZIBs.

APA-NVO nanorods were synthesized *via* a solvothermal method using ammonium metavanadate and amino-PEG-2-amine. A series of pH-dependent experiments (pH = 1–6) were conducted under identical synthesis conditions to investigate the crystallographic and morphological evolution of the samples, designated as APA-NVO*x*, where '*x*' represents the pH value. Field emission scanning electron microscopy (FESEM) and transmission electron microscopy (TEM) were used to analyze the morphology and detailed structure of the synthesized APA-NVO products.

Fig. 1 and Fig. S1 (ESI†) illustrate the variations in crystallinity and morphology at different pH levels. At pH 4, the material exhibited improved crystallinity and a uniform nanorod structure. As shown in Fig. 1a, APA-NVO4 crystallized into uniform nanorods several tens of nanometers wide and a few micrometers long. High-resolution TEM (HRTEM) images (Fig. 1c) reveal an interlayer spacing of 15.2 Å (Fig. 1b and c), corresponding to a 2θ of 5.7° for the APA-NVO4 crystals. The selected-area electron diffraction (SAED) pattern (inset, Fig. 1c) displays the diffraction rings of APA-NVO4, confirming the polycrystalline nature of the nanoribbons. Additionally, scanning transmission electron microscopy with energy-dispersive spectroscopy (STEM-EDS) element mappings (Fig. 1d–h) of a single nanoribbon reveal a uniform distribution of V, O, N, and C elements, indicating the homogeneity of the constituents necessary for forming a high-quality organic–inorganic hybrid structure with the probable mechanism of APA insertion into NVO is shown schematically in Fig. S2 (ESI†).

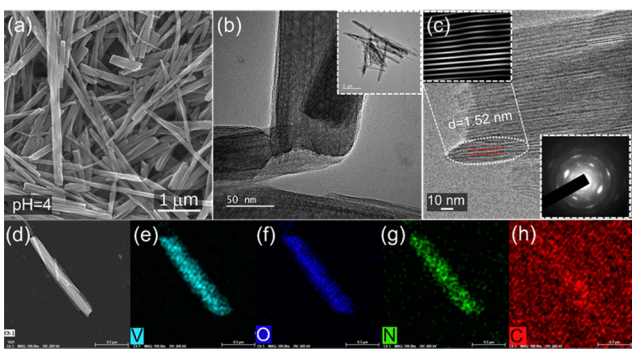

Fig. 1 (a) FESEM and TEM image of (a) and (b) APA-NVO4 nanorods. (c) HR-TEM image, IFFT pattern (inset, left) and the corresponding SAED pattern (inset, right), and (d)–(h) EDS mapping results for selected elements, including V, O, N, and C.

Powder X-ray diffraction (PXRD, Fig. S4a, ESI†) was used to characterize the crystal structure changes induced by APA intercalation in NVO. Both pure NVO and APA-intercalated NVO exhibited monoclinic structures (JCPDS no. 41-0492, $NH_4V_3O_8{\cdot}0.5H_2O$). As expected, the diffraction peak intensities for APA-NVO were lower than those of pure NVO (normalized), likely due to the shielding effect of the organic molecules.[25] An additional notable feature in APA-NVO4 was a negative shift in the intense diffraction peak at 2θ = 11.4° [for the (001) plane in pure NVO] to 2θ = 5.7° and the same is reflected in the HRTEM images (Fig. S3d, ESI†) revealing an interlayer spacing of 7.4 Å. The interplanar spacing in APA-NVO4, calculated using the Bragg equation, increased to 15.7 Å compared to 7.7 Å in pristine NVO after APA intercalation. The Raman spectra (Fig. S4b, ESI†) display a low-frequency vibrational mode at 143.6 cm^{-1}, indicating chain translation related to the layered structure. The mode at 993.0 cm^{-1} corresponds to V═O stretching along the *c*-axis, while modes at 404.4 and 524.1 cm^{-1} are attributed to V–O–V stretching. Peaks at 282.9 and 693.4 cm^{-1} likely reflect the presence of water molecules in NVO.[28] The presence of APA molecules in APA-NVO4 was confirmed by FTIR spectra. As shown in the FTIR spectrum (Fig. S4c, ESI†), characteristic peaks at approximately 1610, 1490, 1330, and 1080 cm^{-1} correspond to the stretching and bending vibrations of N–H, C–H, C–N, and C–O bonds in APA, respectively.[29,30] Overall, the PXRD and spectroscopic results confirm the integration of APA within the V–O layers. Thermogravimetric (TG) analysis (Fig. S4d, ESI†) indicated that the APA-NVO hybrid contained a significant amount of APA (30 wt%) and a minimal quantity of physical/structural water (4 wt%). APA likely acts as a chelating ligand between the V–O layers and may also participate in Zn^{2+} storage in aqueous ZIBs.

The chemical composition and elemental valence states of APA-NVO4 were determined using X-ray photoelectron spectroscopy (XPS). The wide survey spectrum of APA-NVO4 (Fig. S5a, ESI†) confirmed the presence of C, O, N, and V, consistent with the TEM data. High-resolution XPS (Fig. S5b, ESI†) revealed peaks at 515.6 and 514.1 eV (V $2p_{3/2}$) attributed to V^{5+}, and 523.3 and 522.1 eV (V $2p_{1/2}$) corresponding to V^{4+}. In the C 1s spectrum (Fig. S5c, ESI†), peaks at 284.1, 285.5, and 287.9 eV were assigned to C–C, C–N, and C–O–C bonds, respectively. The O 1s XPS region (Fig. S5d, ESI†) was fitted to three peaks corresponding to V–O, OH^-, and O–C.

Among the synthesized materials, APA-NVO4 showed a uniform nanorod morphology, high crystallinity and wider *d*-spacing, so we have chosen it for detailed electrochemical analysis. To evaluate the potential merits of the designed organo-hybrid nanorods in AZIBs, we studied the electrochemical properties in a coin cell (CR 2032) using APA-NVO4 as the cathode, Zn foil as the anode, and a Celgard® separator permeated with an aqueous 3 M $Zn(CH_3F_3SO_3)_2$ electrolyte. The cyclic voltammetry (CV) profiles for the second cycle of both samples at 0.2 mV s^{-1} are shown in Fig. S6 (ESI†). Charge–discharge profiles for cells with different cathode materials, NVO and APA-NVO4, at 100 mA g^{-1} demonstrated specific capacities of 60 and 377 mA h g^{-1}, respectively. The higher capacitance of the APA-NVO4 composite can be

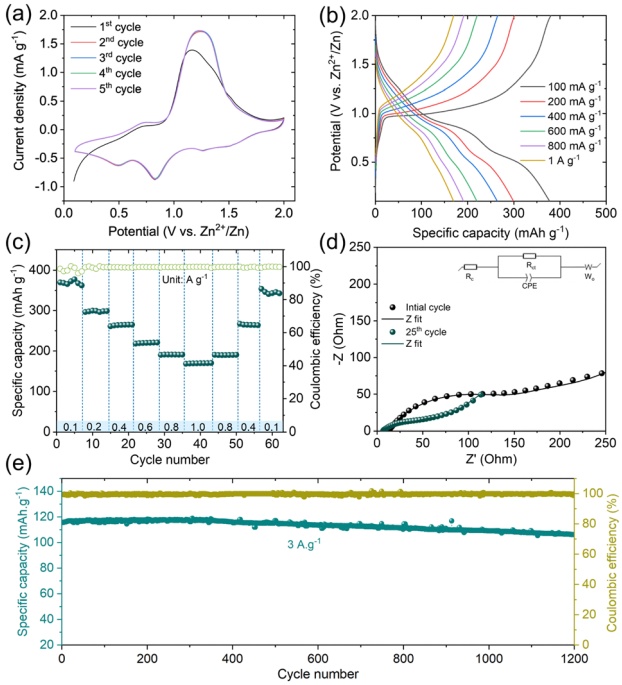

Fig. 2 Electrochemical measurements of APA-NVO4 for aqueous ZIBs. (a) CV curves for the initial five cycles at 0.4 mV s^{-1}, (b) GCD curve of the ZIB at various current rates, and (c) rate capability plot recorded at different current densities, (d) Nyquist plot of the pristine and 25th discharged states (inset EIS circuit), and (e) long-term stability at 3 A g^{-1}.

attributed to the intercalated organic molecules, which increased the interlayer spacing and improved the morphology. Given the superior charge storage capacity of APA-NVO4, a detailed electrochemical study was conducted. Fig. 2a presents the highly reversible CV profiles of the Zn//APA-NVO4 cell during the initial five cycles at 0.4 mV s^{-1}, with a working voltage between 0.1 and 2.0 V. The difference between the initial cycle and subsequent cycles is attributed to the gradual activation of the electrode, enhancing ion mobility at the electrode/electrolyte interfaces and facilitating the (de)intercalation process.

The redox peaks are attributed to the continuous (de)intercalation of Zn^{2+} in the VO layered structure of APA-NVO4, indicating a multistep reaction mechanism. The CV profiles largely overlap, suggesting excellent reversibility of Zn^{2+} (de)intercalation. Typical CV curves for the APA-NVO4 cathode show two pairs of peaks at 1.21/0.83 V and 0.73/0.49 V, corresponding to the redox couples V^{5+}/V^{4+} and V^{4+}/V^{3+}, respectively. The rate performance and corresponding charge/discharge profiles of the APA-NVO4 cathode are illustrated in Fig. 2b and c, with current densities increasing from 0.1 to 1 A g^{-1}, yielding specific discharge capacities of 376.7, 300.0, 263.6, 219.7, 189.7, and 160.0 mA h g^{-1}, respectively. Notably, when the current density is reverted to 0.1 A g^{-1}, a high discharge capacity of 353.7 mA h g^{-1} is recovered, indicating excellent rate capability. Upon cycling, the charge transfer resistance decreases, as shown in the EIS analysis (Fig. 2d). The fresh APA-NVO4 electrode exhibits an equivalent series resistance (ESR) of 12 Ω and a large charge-transfer resistance (R_{ct}) of 155 Ω. After 25 cycles, the ESR decreases to 6.4 Ω, and the R_{ct} reduces to 45.6 Ω. The long-term cycling stability of the APA-NVO4 cathode is shown in Fig. 2e. At a current density of 1 A g^{-1}, the electrode demonstrates a high reversible capacity of 164.0 mA h g^{-1} and good capacity retention after 200 cycles (Fig. S7, ESI†). Even at a high current density of 3 A g^{-1}, the APA-NVO4 electrode delivers a capacity of 105 mA h g^{-1} after 1200 cycles, achieving a coulombic efficiency of nearly 100% with only 9% capacity fading, demonstrating superior cycling stability.

The electrochemical kinetic performance was assessed, as illustrated in Fig. S8a (ESI†), through cyclic voltammetry (CV) curves recorded at various scan rates. The relationship between the peak current (i) and the scan rate (ν) is described by eqn (1) and (2).[31]

$$i = a\nu^b \quad (1)$$

$$\log i = b \log \nu + \log a \quad (2)$$

where 'a' and 'b' are variable parameters. A 'b' value close to ~0.5 indicates a diffusion-limited charge storage process, typical of solid-state intercalation reactions in layered materials. Conversely, a 'b' value near ~1.0 suggests that Zn^{2+} storage is dominated by surface-induced capacitive charge transfer processes at or near the electrode surface.[32] The calculated 'b' values for the four redox peaks were observed at 0.56, 0.89, 0.57, and 0.56, respectively, indicating predominantly diffusion-controlled kinetics (Fig. S8b, ESI†) in our case.

The contribution of diffusion-controlled charge–discharge capacity can be quantified using eqn (3).

$$i = k_1\nu + k_2\nu^{1/2} \quad (3)$$

In this equation, $k_1\nu$ represents the capacitive contribution and $k_2\nu^{1/2}$ reflects the diffusion-controlled contribution. Fig. S8c (ESI†) shows that the diffusive contribution was 79.6% at 0.8 mV s^{-1} for APA-NVO4. As the sweep rate increased, the capacitive effect became more significant, rising from 11.3% at 0.2 mV s^{-1} to 28.8% at 2.0 mV s^{-1} (Fig. S8d, ESI†). This increase is attributed to the surface-induced pseudocapacitive mechanism of the APA-NVO4 cathode. The 2D nanorod morphology of APA-NVO4 provides numerous Zn^{2+} adsorption/desorption sites and facilitates charge transfer during discharge–charge cycles, enhancing electrochemical storage performance. The improved Zn^{2+} diffusion rate and optimized electrochemical kinetics are crucial for achieving superior electrochemical performance in aqueous ZIBs.

To further elucidate the Zn^{2+} storage mechanism in APA-NVO4, *ex situ* analysis was conducted to investigate structural evolution during the initial galvanostatic discharge cycles. Fig. S9 (ESI†) shows the *ex situ* XRD patterns of the cathode materials at different states in the Zn//$(NH_4)V_3O_8$ battery at 0.1 A g^{-1}, disclosing the evolution of the crystal structure during the charge/discharge process. *Ex situ* high-resolution XPS analysis at the discharge state confirmed the intercalation of metal ions and their interaction with cathode elements. The XPS full spectrum of APA-NVO4 revealed the presence of C, O, N, V, and Zn, indicating metal ion insertion during discharge (Fig. S10a, ESI†). As shown in Fig. S10b (ESI†), peaks at 515.6,

514.1 eV (V $2p_{3/2}$), and 523.3, 522.1 eV (V $2p_{1/2}$) correspond to V^{5+} and V^{4+}, respectively. Upon Zn^{2+} insertion, the vanadium valence is reduced, with new peaks at 515.1 and 522.4 eV indicating the presence of V^{3+} at the discharge state. The core-level Zn 2p spectra (Fig. S10c, ESI†) display prominent peaks at 1044.7 eV (Zn $2p_{1/2}$) and 1021.6 eV (Zn $2p_{3/2}$), confirming Zn^{2+} intercalation into the cathode material.[28] Additionally, the *ex situ* high-resolution C 1s XPS spectra (Fig. S10d, ESI†) show peaks at 284.5, 286.5, 289.7, and 291.7 eV, corresponding to C–C, C–N, C–O–C, and C–F bonds, respectively. The post-durability analysis of the cathode was carried out to gain an insight during the cycling stability. *Ex situ* XRD, after 1000 cycles at 2.0 V, is nearly similar to that at the 1st cycle, demonstrating the structural stability of the $(NH_4)V_3O_8$ after the phase transformation (Fig. S11a, ESU). FESEM and TEM images at different states revealed an insignificant change in the rod-shaped morphology; however, slight aggregation is noticed after cycling, which could be the reason for the decay in capacity (Fig. S11b–e, ESI†).

In summary, a hybrid inorganic–organic material (APA-NVO) was synthesized *via* a solvothermal method and evaluated as a cathode for aqueous ZIBs. This material utilizes a dual energy-storage mechanism stemming from the vanadium oxide layer and APA, achieving a high working voltage due to the organic component while maintaining the high capacity and long cycling life due to vanadium oxide. The APA-NVO cathode demonstrated a specific capacity of 376.6 mA h g^{-1} at 0.1 A g^{-1} and exceptional cycling stability, with 94% capacity retention after 1200 cycles at 3 A g^{-1}. Characterization techniques, including TEM, XRD, XPS, and FTIR, alongside *ex situ* XPS results, confirmed the successful intercalation of APA within the NVO layers and the highly reversible nature of the charge–discharge reactions. This work presents a strategy for harnessing the benefits of organic and inorganic components in a nanohybrid, potentially accelerating the development of high-energy cathodes for aqueous ZIBs.

Data availability

The data supporting this article is provided in the ESI.†

Conflicts of interest

There are no conflicts to declare.

References

1 C. Liu, F. Li, L.-P. Ma and H.-M. Cheng, *Adv. Mater.*, 2010, **22**, E28–E62.
2 W. Tang, Y. Zhu, Y. Hou, L. Liu, Y. Wu, K. P. Loh, H. Zhang and K. Zhu, *Energy Environ. Sci.*, 2013, **6**, 2093–2104.
3 M. Armand and J. M. Tarascon, *Nature*, 2008, **451**, 652–657.
4 C. Xu, B. Li, H. Du and F. Kang, *Angew. Chem., Int. Ed.*, 2012, **124**, 957–959.
5 M.-C. Lin, M. Gong, B. Lu, Y. Wu, D.-Y. Wang, M. Guan, M. Angell, C. Chen, J. Yang, B.-J. Hwang and H. Dai, *Nature*, 2015, **520**, 324–328.
6 B. Ji, F. Zhang, M. Sheng, X. Tong and Y. Tang, *Adv. Mater.*, 2017, **29**, 1604219.
7 P. Qin, M. Wang, N. Li, H. Zhu, X. Ding and Y. Tang, *Adv. Mater.*, 2017, **29**, 1606805.
8 H. Pan, Y. Shao, P. Yan, Y. Cheng, K. S. Han, Z. Nie, C. Wang, J. Yang, X. Li, P. Bhattacharya, K. T. Mueller and J. Liu, *Nat. Energy*, 2016, **1**, 16039.
9 X. Wang, F. Wang, L. Wang, M. Li, Y. Wang, B. Chen, Y. Zhu, L. Fu, L. Zha, L. Zhang, Y. Wu and W. Huang, *Adv. Mater.*, 2016, **28**, 4904–4911.
10 S. Zafar and B. Lochab, *ACS Omega*, 2024, **9**, 47920–47938.
11 J. Huang, Z. Wang, M. Hou, X. Dong, Y. Liu, Y. Wang and Y. Xia, *Nat. Commun.*, 2018, **9**, 2906.
12 W. Deng, Z. Li, Y. Ye, Z. Zhou, Y. Li, M. Zhang, X. Yuan, J. Hu, W. Zhao, Z. Huang, C. Li, H. Chen, J. Zheng and R. Li, *Adv. Energy Mater.*, 2021, **11**, 2003639.
13 S. Zafar, S. K. Singh and B. Lochab, *Mater. Adv.*, 2023, **4**, 2425–2436.
14 S. Zhang, H. Tan, X. Rui and Y. Yu, *Acc. Chem. Res.*, 2020, **53**, 1660–1671.
15 H. Tang, Z. Peng, L. Wu, F. Xiong, C. Pei, Q. An and L. Mai, *Electrochem. Energy Rev.*, 2018, **1**, 169–199.
16 J. Cao, D. Zhang, C. Gu, X. Wang, S. Wang, X. Zhang, J. Qin and Z.-S. Wu, *Adv. Energy Mater.*, 2021, **11**, 2101299.
17 X. Zhao, L. Mao, Q. Cheng, F. Liao, G. Yang, X. Lu and L. Chen, *Energy Storage Mater.*, 2021, **38**, 397–437.
18 H. Jiang, Y. Zhang, L. Xu, Z. Gao, J. Zheng, Q. Wang, C. Meng and J. Wang, *Chem. Eng. J.*, 2020, **382**, 122844.
19 Y. Zhang, H. Jiang, L. Xu, Z. Gao and C. Meng, *ACS Appl. Energy Mater.*, 2019, **2**, 7861–7869.
20 F. Wan, L. Zhang, X. Wang, S. Bi, Z. Niu and J. Chen, *Adv. Funct. Mater.*, 2018, **28**, 1804975.
21 K. Qin, J. Huang, K. Holguin and C. Luo, *Energy Environ. Sci.*, 2020, **13**, 3950–3992.
22 Z. Tie and Z. Niu, *Angew. Chem., Int. Ed.*, 2020, **59**, 21293–21303.
23 J. Cui, Z. Guo, J. Yi, X. Liu, K. Wu, P. Liang, Q. Li, Y. Liu, Y. Wang, Y. Xia and J. Zhang, *ChemSusChem*, 2020, **13**, 2160–2185.
24 Z. Guo, Y. Ma, X. Dong, J. Huang, Y. Wang and Y. Xia, *Angew. Chem., Int. Ed.*, 2018, **130**, 11911–11915.
25 D. Bin, W. Huo, Y. Yuan, J. Huang, Y. Liu, Y. Zhang, F. Dong, Y. Wang and Y. Xia, *Chem*, 2020, **6**, 968–984.
26 S. Liu, H. Zhu, B. Zhang, G. Li, H. Zhu, Y. Ren, H. Geng, Y. Yang, Q. Liu and C. C. Li, *Adv. Mater.*, 2020, **32**, 2001113.
27 S. Zafar, M. Sharma, K. Shai Mp, N. Karmodak, S. K. Singh and B. Lochab, *J. Mater. Chem. A*, 2024, **12**, 32947–32956.
28 T. Wei, Q. Li, G. Yang and C. Wang, *J. Mater. Chem. A*, 2018, **6**, 20402–20410.
29 C. V. S. Reddy, J. Wei, Z. Quan-Yao, D. Zhi-Rong, C. Wen, S.-I. Mho and R. R. Kalluru, *J. Power Sources*, 2007, **166**, 244–249.
30 T. Hu, Z. Li, L. Lu, K. Dai, J. Zhang, R. Li and C. Liang, *J. Colloid Interface Sc.*, 2019, **555**, 166–173.
31 X. Zhu, Z. Cao, X.-L. Li, L. Pei, J. Jones, Y.-N. Zhou, P. Dong, L. Wang, M. Ye and J. Shen, *Energy Storage Mater.*, 2022, **45**, 568–577.
32 F. Yu, T. Huang, P. Zhang, Y. Tao, F.-Z. Cui, Q. Xie, S. Yao and F. Wang, *Energy Storage Mater.*, 2019, **22**, 235–255.

